This is the peer-reviewed, final accepted version for American Mineralogist, published by the Mineralogical Society of America.
The published version is subject to change. Cite as Authors (Year) Title. American Mineralogist, in press.
DOI: https://doi.org/10.2138/am-2020-7540. http://www.minsocam.org/

Revision 1

Seaborgite, $LiNa_6K_2(UO_2)(SO_4)_5(SO_3OH)(H_2O)$, the first uranyl mineral containing lithium

ANTHONY R. KAMPF[1§], TRAVIS A. OLDS[2], JAKUB PLÁŠIL[3], JOE MARTY[4] , SAMUEL N. PERRY[5], LORETTA CORCORAN[5] AND PETER C. BURNS[5,6]

[1] Mineral Sciences Department, Natural History Museum of Los Angeles County, 900 Exposition Boulevard, Los Angeles, CA 90007, USA

[2] Section of Minerals and Earth Sciences, Carnegie Museum of Natural History, 4400 Forbes Avenue, Pittsburgh, Pennsylvania 15213, USA

[3] Institute of Physics ASCR, v.v.i., Na Slovance 1999/2, 18221 Prague 8, Czech Republic

[4] 5199 East Silver Oak Road, Salt Lake City, UT 84108, USA

[5] Department of Civil and Environmental Engineering and Earth Sciences, University of Notre Dame, Notre Dame, IN 46556, USA

[6] Department of Chemistry and Biochemistry, University of Notre Dame, Notre Dame, IN 46556, USA

ABSTRACT

Seaborgite (IMA2019-087), $LiNa_6K_2(UO_2)(SO_4)_5(SO_3OH)(H_2O)$, is a new mineral species from the Blue Lizard mine, Red Canyon, San Juan County, Utah, U.S.A. It is a secondary phase found on gypsum in association with copiapite, ferrinatrite, ivsite, metavoltine, and römerite. Seaborgite occurs in sprays of light-yellow, long flattened prisms or blades, up to about 0.2 mm in length.

§ Email: akampf@nhm.org

Crystals are elongated on [100], flattened on {010}, and exhibit the forms {100}, {010}, {001}, and {10-1}. The mineral is transparent with vitreous luster and very pale-yellow streak. It exhibits bright lime-green fluorescence under a 405 nm laser. The Mohs hardness is ~2½. The mineral has brittle tenacity, curved or conchoidal fracture, and one good cleavage on {100}. The measured density is 2.97(2) $g \cdot cm^{-3}$. The mineral is immediately soluble in RT H_2O. The mineral is optically biaxial (–), $\alpha = 1.505(2)$, $\beta = 1.522(2)$, $\gamma = 1.536(2)$ (white light); $2V_{meas} = 85(1)°$; moderate $r < v$ dispersion; orientation X ^ **a** ≈ 10°; pleochroic X colourless, Y and Z light green-yellow; $X < Y \approx Z$. Seaborgite EPMA and LA-ICP-MS analyses undermeasured Li, K, and Na. The empirical formula using Li, Na, and K based on the structure refinement is $Li_{1.00}Na_{5.81}K_{2.19}(UO_2)(SO_4)_5(SO_3OH)(H_2O)$. Seaborgite is triclinic, $P\bar{1}$, $a = 5.4511(4)$, $b = 14.4870(12)$, $c = 15.8735(15)$ Å, $\alpha = 76.295(5)$, $\beta = 81.439(6)$, $\gamma = 85.511(6)°$, $V = 1203.07(18)$ $Å^3$, and $Z = 2$. The structure ($R_1 = 0.0377$ for 1935 $I > 2\sigma I$) contains $[(UO_2)_2(SO_4)_8]^{4-}$ uranyl-sulfate clusters that are linked into a band by bridging LiO_4 tetrahedra. The bands are linked through peripheral SO_4 tetrahedra forming a thick heteropolyhedral layer. Channels within the layers contain a K site, while an additional K site, six Na sites, and an SO_3OH group occupy the space between the heteropolyhedral layers.

Keywords: seaborgite; new mineral species; lithium; uranyl sulfate; crystal structure; Blue Lizard mine, Red Canyon, Utah.

INTRODUCTION

The Blue Lizard mine in Red Canyon, Utah is a remarkable source of new minerals, especially sodium-uranyl sulfates. The astounding diversity and relatively high structural

complexity of uranyl-sulfate minerals was recently emphasized by Gurzhiy and Plášil (2019). A large number of stable combinatorial linkages of uranyl and sulfate tetrahedra are possible, with the topological arrangements appearing to be strongly affected by at least three parameters: pH (Plášil et al. 2014), cation content, and water content. In general, sodium-uranyl-sulfate minerals follow the same structural unit topology trends as do other uranyl minerals (Lussier et al. 2016), where uranyl polyhedra preferentially polymerize into extended structures *via* linkages through their equatorial vertices, most often forming infinite chain or infinite sheet topologies. However, finite cluster topologies are relatively abundant among the sodium-uranyl-sulfate minerals, for reasons that are not completely clear. Understanding the hierarchical arrangements of these structures and how conditions of formation influence the crystallized topologies is important to understanding the crystal-chemical nature of U-S systems, and for uranyl mineralogy as a whole.

The new Blue-Lizard-mine uranyl sulfate seaborgite, described herein, contains essential sodium; however, it also includes essential potassium and, most significantly, lithium. While sodium and, especially potassium, form relatively weak bonds within such structures, the role of lithium is rather different. Lithium-oxygen bonds, particularly in LiO_4 tetrahedral coordination, are somewhat stronger and, in the seaborgite structure, serve to further link (or polymerize) the uranyl sulfate clusters.

Seaborgite is named in honor of American chemist Glenn T. Seaborg (1912–1999) who was involved in the synthesis, discovery, and investigation of 10 transuranium elements (including seaborgium), earning him a share of the 1951 Nobel Prize in Chemistry. Seaborg's scientific accomplishments are numerous and changed the course of world history. Perhaps most notably, Seaborg and coworkers discovered plutonium in 1940 and he isolated the first weighable sample of plutonium in 1942. The Manhattan Project produced the first plutonium-fueled nuclear

bomb that was detonated in New Mexico at the Trinity test site on July 16, 1945. Seaborg served as Chairman of the United States Atomic Energy Commission from 1961 to 1971 during which time he worked to advance nuclear energy. Seaborg was a strong proponent for arms control and the peaceful use of nuclear energy.

The new mineral and name were approved by the Commission on New Minerals, Nomenclature and Classification of the International Mineralogical Association (IMA 2019-087). One holotype specimen of seaborgite is deposited in the collections of the Natural History Museum of Los Angeles County, Los Angeles, California, USA, catalogue number 74163.

OCCURRENCE

Seaborgite was found underground in the Blue Lizard mine (37°33'26"N 110°17'44"W), Red Canyon, White Canyon District, San Juan County, Utah, USA. The mine is about 72 km west of the town of Blanding, Utah, and about 22 km southeast of Good Hope Bay on Lake Powell. Detailed historical and geologic information on the Blue Lizard mine is described elsewhere (cf. Kampf et al. 2015), and is primarily derived from a report by Chenoweth (1993).

Abundant secondary uranium mineralization in Red Canyon is associated with post-mining oxidation of asphaltum-rich sandstone beds laced with uraninite and sulfides in the damp underground environment. Seaborgite was found in an area rich in K-bearing sulfates (e.g. metavoltine, voltaite, zincovoltaite), along with several other potentially new sodium and potassium uranyl sulfate minerals. Potassium enrichment has so far not been observed in secondary uranyl mineralization elsewhere in the Blue Lizard mine nor in any of the nearby U deposits in Red Canyon that we have investigated and this is the first uranyl mineral found that contains essential Li. It seems likely that K and Li are sourced from Li- and K-bearing clays in

the sediments.

Seaborgite is a very rare mineral in the secondary mineral assemblages of the Blue Lizard mine. It occurs on a thick crust of gypsum overlaying matrix comprised mostly of subhedral to euhedral, equant quartz crystals that are recrystallized counterparts of the original grains of the sandstone. Other secondary phases found in close association with seaborgite are copiapite, ferrinatrite, ivsite, metavoltine, römerite, and other potentially new uranyl sulfate minerals.

PHYSICAL AND OPTICAL PROPERTIES

Crystals of seaborgite are long flattened prisms or blades, up to about 0.2 mm in length, typically in radiating sprays (Fig. 1). Crystals are elongated on [100], flattened on {010}, and exhibit the forms {100}, {010}, {001}, and {10-1} (Fig. 2). Twinning was observed optically under crossed polars, and is either by reflection on {001} or by rotation around [001].

The mineral is light yellow and transparent with vitreous luster and very pale-yellow streak. Seaborgite exhibits bright lime-green fluorescence under a 405 nm laser. It has a Mohs hardness of about 2½ based on scratch tests. The mineral has brittle tenacity, curved or conchoidal fracture, and one good cleavage on {100}. The density measured by flotation in a mixture of methylene iodide and toluene is 2.97(2) $g \cdot cm^{-3}$. The calculated density is 3.015 $g \cdot cm^{-3}$ for the empirical formula (using Li, Na, and K based on the structure refinement) and single-crystal cell; 3.004 $g \cdot cm^{-3}$ for the ideal formula. The mineral is immediately soluble in H_2O at room temperature.

Seaborgite is optically biaxial (–) with $\alpha = 1.505(2)$, $\beta = 1.522(2)$, $\gamma = 1.536(2)$ measured in white light. The $2V$ measured using extinction data analyzed with EXCALIBRW (Gunter et al. 2004) is 85(1)°; the calculated $2V$ is 83.6°. The dispersion is moderate, $r < v$. The partially

116 determined optical orientation is X ^ **a** ≈ 10°. Crystals are pleochroic with X colourless, Y and Z
117 light green-yellow; $X < Y \approx Z$. The Gladstone–Dale compatibility, $1 - (K_P/K_C)$, (Mandarino 2007)
118 is -0.009 (superior) based on the empirical formula (using Li, Na, and K based on the structure
119 refinement) using $k(UO_3) = 0.118$, as provided by Mandarino (1976).
120

121 ## RAMAN SPECTROSCOPY

122 Raman spectroscopy was conducted on a Horiba XploRA PLUS using a 532 nm diode
123 laser, 50 μm slit, 2400 gr/mm diffraction grating, and a 100× (0.9 NA) objective. The spectrum,
124 recorded from 4000 to 100 cm^{-1}, is shown in Figure 3.
125 Two weak bands with centers at 3570 and 3475 cm^{-1} are assigned to ν(OH) stretching
126 vibrations. Using the empirically derived equation of Libowitzky (1999) the calculated O···O
127 distances of the corresponding hydrogen bonds are between ~3.0 Å and ~2.8 Å, in reasonable
128 agreement with the hydrogen bond lengths determined from the structure refinement. Several
129 very broad low intensity bands centered at ~2600 and ~1800 cm^{-1} are probably overtones or
130 combination bands. No apparent band related to the $\nu_2(\delta)$ bending vibrations of H_2O, is present at
131 approximately 1600 cm^{-1}, which is not surprising considering the low sensitivity of Raman for
132 the non-symmetrical vibrations.
133 There has been no reliable computational/theoretical research focused on differentiating
134 SO_4 and SO_3OH in Raman spectra; therefore, our assignments of the vibrations connected with
135 the sulfate tetrahedra in seaborgite are tentative. The $\nu_3(SO_4/SO_3OH)$ antisymmetric stretching
136 vibrations occur as weak bands at 1203, 1194, 1173, 1139, and 1091 cm^{-1}. Several weak to
137 strong bands at 1045, 1026, 1015, 1002, and 979 cm^{-1} are assignable to the ν_1 symmetric
138 stretching vibrations of SO_4 and SO_3OH groups. The presence of six symmetrically unique SO_4

tetrahedra in the seaborgite structure lead to the multiple split bands in this region. The weak band at 917 cm^{-1} is related to the $\nu_3(UO_2)^{2+}$ antisymmetric stretching vibration, while the band at 885 cm^{-1} is assigned to the ν(S–OH) mode (cf. Plášil et al. 2013). The $\nu_1(UO_2)^{2+}$ symmetric stretching vibration is present as a very strong band at 850 cm^{-1}. Bartlett and Cooney (1989) provided an empirical relationship to derive the approximate U–O_{Ur} bond lengths from the band position assigned to the UO_2^{2+} stretching vibrations, which gives 1.76 Å (ν_1) and 1.77 Å (ν_3), in excellent agreement with the average U1–O_{Ur} bond length from the X-ray data: 1.757 Å. At least seven overlapping weak bands between 657 and 586 cm^{-1} are attributable to the $\nu_4(\delta)(SO_4/SO_3OH)$ bending vibrations, with centers at 657, 647, 641, 634, 621, 605, and 586 cm^{-1}. Those at 479, 463, 444, and 425 cm^{-1} belong to the $\nu_2(\delta)(SO_4/SO_3OH)$ bending vibrations. A band at 250 cm^{-1} is attributable to the $\nu_2(\delta)(UO_2)^{2+}$ bending vibrations and/or possibly to ν(U–O_{eq}) bending modes. The remaining bands arise due to unassigned phonon modes.

CHEMICAL ANALYSIS

Chemical analyses for all elements except Li (8 points on 2 crystals) were performed on a JEOL JXA-8230 electron microprobe using Probe for EPMA software. The analytical conditions used were 10 keV accelerating voltage, 10 nA beam current, and a beam diameter of 10 μm. Raw X-ray intensities were corrected for matrix effects with a $\phi\rho(z)$ algorithm (Pouchou and Pichoir 1991). Time-dependent intensity corrections were applied to data for Na and K. No other elements were detected by EDS and wavescans at multiple currents and beam sizes showed no N above background. Crystals of seaborgite experienced considerable damage under the electron beam. The amount of Na, and to a lesser extent K, reported in the EPMA are significantly lower

than those based on the structure refinement; this is attributed to the failure of the time-dependent intensity corrections to fully account for the volatility of Na and K.

Li, Na, and U were measured using Laser Ablation Inductively Coupled Plasma Mass Spectrometry (LA-ICP-MS). The ion signals for Li, Na, and U from 2 crystal aggregates were measured using an Element 2 sector field high resolution inductively coupled plasma mass spectrometer (Thermo Fisher Scientific) in low mass resolution mode coupled with a UP-213 (New Wave Research) Nd:YAG deep UV (213 nm) laser ablation system. Prior to the ablation of samples, the Element 2 was tuned using a multi-element solution containing 1 $ng \cdot g^{-1}$ of each Li, In, and U to obtain maximum ion sensitivity. The laser ablation analyses involved acquiring background ion signals for 60 seconds with the laser on and shuttered, and this was followed by 60 seconds of data acquisition. The laser was operated using a 30 μm spot size, repetition rate of 5 Hz, and 65% power output, which corresponded to a fluence of ~8.4 $J \cdot cm^{-2}$. Two areas on two crystals were examined using single spot analyses. The background corrected ion signals (counts per second) obtained for Li, Na, and U are reported as an atomic ratio relative to that recorded for U, which was used to calculate a corresponding wt% oxide value, as absolute abundances could not be determined due to a lack of an appropriate matrix-matched external standard. The analytical value obtained for Na, while higher than that obtained by EPMA, is also significantly lower than that based on the structure refinement, as is the value obtained for Li; the "undermeasurements" are probably due to the fact that we cannot adequately account for the ionization efficiency differences.

Because insufficient material is available for a direct determination of H_2O, it has been calculated based upon the structure determination (U+S = 7 *apfu*, O = 27 *apfu*). Analytical data are given in Table 1. The empirical formula using Na measured via EPMA is

184 $Li_{0.79}Na_{5.02}K_{2.02}(UO_2)(SO_4)_5(SO_3OH)(H_2O)$, which has a charge deficiency of 1.17 due to
185 undermeasurements of Li, K, and Na. The empirical formula using Na measured via LA-ICP-MS
186 is $Li_{0.79}Na_{5.19}K_{2.02}(UO_2)(SO_4)_5(SO_3OH)(H_2O)$, which has a charge deficiency of 1.00 due to
187 undermeasurements of Li, K, and Na. The empirical formula using Li, Na, and K based on the
188 structure refinement is $Li_{1.00}Na_{5.81}K_{2.19}(UO_2)(SO_4)_5(SO_3OH)(H_2O)$. The simplified formula is
189 $LiNa_5(Na,K)K_2(UO_2)(SO_4)_5(SO_3OH)(H_2O)$ and the ideal formula is
190 $LiNa_6K_2(UO_2)(SO_4)_5(SO_3OH)(H_2O)$, which requires Li_2O 1.37, Na_2O 17.08, K_2O 8.65, UO_3
191 26.28, SO_3 44.13, H_2O 2.48, total 100 wt%.
192

193 ## X-RAY CRYSTALLOGRAPHY AND STRUCTURE DETERMINATION

194 Both powder and single-crystal X-ray studies were carried out using a Rigaku R-Axis
195 Rapid II curved imaging plate microdiffractometer with monochromatized Mo*K*α radiation. For
196 the powder study, a Gandolfi-like motion on the φ and ω axes was used to randomize the sample,
197 which consisted of several crystals. Observed *d* values and intensities were derived by profile
198 fitting using JADE 2010 software (Materials Data, Inc. Livermore, CA). Data are given in
199 Supplemental[1] Table S1. The observed powder diffraction pattern compares very well with the
200 pattern calculated from the crystal structure (Fig. 4)
201 The relatively small crystal size only allowed structure data to be collected to 40° 2θ;
202 consequently, the data to parameter ratio (5.45) was less than optimal. The Rigaku CrystalClear
203 software package was used for processing the structure data, including the application of an
204 empirical absorption correction using the multi-scan method with ABSCOR (Higashi 2001). The
205 structure was solved by the charge-flipping method using SHELXT (Sheldrick 2015a). SHELXL-
206 2016 (Sheldrick 2015b) was used for the refinement of the structure.

A cation site with scattering power, coordination, bond lengths, and bond valence appropriate for Li was located. (The presence of Li was independently confirmed by LA-ICP-MS.) Nine cation sites other than S, H, and U were located. Two fully occupied by K (K1 and K2), five fully occupied by Na (Na1 thru Na5), one split Na site (Na6a and Na6b) and one occupied jointly by Na and K (Na/K), which refined to $Na_{0.62}K_{0.38}$. All non-hydrogen atoms were successfully refined with anisotropic displacement parameters, but several O sites exhibited strongly oblate and/or prolate ellipsoids. This may indicate some local disorder (or local "flexibility") in the structure, but splitting of the sites did not appear warranted. At least some of the ellipsoid anisotropy may be due to inadequacies in the empirical absorption correction, although a shape-based absorption correction yielded a higher R_{int} and did not lessen the ellipsoid anisotropies.

Difference-Fourier syntheses located all H atom positions associated with the H_2O groups, which were then refined with soft restraints of 0.82(3) Å on the O–H distances and 1.30(3) Å on the H–H distances and with the U_{eq} of the OH H atom set to 1.5 times the OH O atom and that for each H_2O H atom set to 1.2 times that of the H_2O O atom. The crystallographic data can be found in the original CIF (as supplementary file[1]). Selected bond distances are given in Table 2 and a bond-valence analysis in Table 3.

DISCUSSION

The U site in the structure of seaborgite is surrounded by seven O atom sites forming a squat pentagonal bipyramid. This is a typical coordination for U^{6+} in which the two short apical bonds of the bipyramid constitute the uranyl group (cf. Burns, 2005). The two apical O atoms of the bipyramids (O_{Ur}) form short bonds with the U, and this unit comprises the UO_2^{2+} uranyl

group. Five equatorial O atoms (O_{eq}) complete the U coordination. All O_{eq} atoms also participate in SO_4 groups. The UO_7 bipyramid is surrounded by five SO_4 tetrahedra centered by S1(×2), S2, S3, and S4, each of which shares one O_{eq} corner of the UO_7 bipyramid. One additional SO_4 tetrahedron (centered by S5) and one SO_3OH tetrahedron (centred by S6) are not linked to the UO_7 bipyramid.

The UO_7 bipyramids are linked to one another by pairs of $S1O_4$ tetrahedra to form a $[(UO_2)_2(SO_4)_8]^{4-}$ uranyl-sulfate cluster, which is topologically identical to the cluster in the structure of bluelizardite, $Na_7(UO_2)(SO_4)_4Cl(H_2O)_2$ (Plášil et al. 2014); the two clusters differ in the relative rotation of 1- and 2-connected tetrahedra only, so they can be transformed one into another without the breaking of chemical bonds (Fig. 4). The Li is in regular tetrahedral coordination, typical for Li. Each of the vertices of the LiO_4 tetrahedron is shared with an SO_4 tetrahedron (2× $S2O_4$ and 2× $S5O_4$). Two LiO_4 tetrahedra and two $S2O_4$ tetrahedra form a four-member corner-sharing $(LiO_2)_2(S2O_4)_2$ ring in the {100} plane; the $[(UO_2)_2(SO_4)_8]^{4-}$ uranyl-sulfate clusters and the $(LiO_2)_2(S2O_4)_2$ rings link through the $S2O_4$ tetrahedra to form a band lying in the {100} plane and extending along [010] (Fig. 5). The $S5O_4$ tetrahedra form links in the [100] direction between LiO_4 tetrahedra in adjacent bands. The UO_7 pentagonal bipyramids, LiO_4 tetrahedra, and SO_4 tetrahedra (centered by S1 through S5) thereby form a thick heteropolyhedral layer parallel to {001} (Fig. 6). The $S6O_3OH$ tetrahedron does not participate in this layer linkage.

The two K sites (K1 and K2) are both eight coordinated, as is the mixed Na/K site. The Na1, Na2, Na4, and Na5 sites are six coordinated, the Na3 site is seven coordinated and the split Na6 sites (Na6a and Na6b) are each five coordinated. All bond valence sums (Table 7) for these large monovalent cation sites are reasonable. The K1 site is located at the center of channels that

run through the center of the heteropolyhedral layer. The other large cation sites K2, NaK, Na1, Na2, Na3, Na4, and Na5, as well as the $S6O_3OH$ tetrahedron and the OW27 H_2O group occupy the space between and around the periphery of the heteropolyhedral layers with bonding between them resulting in a framework (Fig. 7). Among all structures containing U^{6+}, that of seaborgite is unique.

Nevertheless, in spite of the structural uniqueness of seaborgite, it is noteworthy that its structural complexity, $I_{G,total}$ = 510.17 bits/cell (after Krivovichev 2012, 2013, 2014, 2018), falls within the most frequent range of complexities observed for uranyl sulfates, 500 to 600 bits/cell (Gurzhiy and Plášil 2019).

IMPLICATIONS

Seaborgite is the first uranyl mineral that contains structurally essential lithium, although many synthetic inorganic compounds contain both lithium and uranium. Only two synthetic uranyl sulfates contain lithium, and these are exotic nanoscale cage cluster compounds (Qiu et al. 2017). In seaborgite, the lithium cations are in tetrahedral coordination with the four oxygen atoms contributed by monodentate sulfate tetrahedra. Whereas the fundamental building blocks consisting of uranyl dimers connected to eight sulfate tetrahedra in seaborgite have been observed in other minerals and synthetic compounds, the presence of the lithium-centered tetrahedra stitches these together with additional sulfate tetrahedra to form highly unique uranyl sulfate layers. Within these layers are infinite rods consisting of lithium and sulfate tetrahedra that are made possible by the small size of the lithium cation. The large hydrated radius of lithium that consists of two hydration spheres and its high enthalpy of hydration indicate it is unlikely that extended uranyl sulfate units containing lithium polyhedra exist in the aqueous solution from

276 which seaborgite crystallized. Incorporation of lithium tetrahedra in the structure of seaborgite
277 occurred during crystallization caused by evaporation likely close to dryness, and the uncommon
278 coexistence of sufficient uranyl ions and lithium cations in the same natural aqueous solution
279 combined to produce this unusual mineral and its corresponding structure.
280

281 ## ACKNOWLEDGEMENTS

282 Sergey Krivovichev, an anonymous reviewer and the Technical Editor are thanked for
283 constructive comments, which improved the manuscript. Associate Editor G. Diego Gatta is
284 thanked for shepherding the manuscript through the review process. Funding to the University of
285 Notre Dame was provided by the Chemical Sciences, Geosciences and Biosciences Division,
286 Office of Basic Energy Sciences, Office of Science, U.S. Department of Energy, Grant No. DE-
287 FG02-07ER15880. Funding to JP was provided by the Czech Science Foundation (20-11949S).
288 This study was also funded by the John Jago Trelawney Endowment to the Mineral Sciences
289 Department of the Natural History Museum of Los Angeles County.
290

291 ## REFERENCES

292 Bartlett, J.R., and Cooney, R.P. (1989) On the determination of uranium-oxygen bond lengths in
293 dioxouranium(VI) compounds by Raman spectroscopy. Journal of Molecular Structure, 193,
294 295–300.
295 Burns, P.C. (2005) U^{6+} minerals and inorganic compounds: Insights into an expanded structural
296 hierarchy of crystal structures. The Canadian Mineralogist, 43, 1839–1894.

297 Chenoweth, W.L. (1993) The Geology and Production History of the Uranium Deposits in the
298 White Canyon Mining District, San Juan County, Utah. Utah Geological Survey
299 Miscellaneous Publication, 93–3.
300 Ferraris, G., and Ivaldi, G. (1988) Bond valence vs bond length in O···O hydrogen bonds. Acta
301 Crystallographica, B44, 341–344.
302 Gagné, O.C., and Hawthorne, F.C (2015) Comprehensive derivation of bond-valence parameters
303 for ion pairs involving oxygen. Acta Crystallographica, B71, 562–578.
304 Gunter, M.E., Bandli, B.R., Bloss, F.D., Evans, S.H., Su, S.C., and Weaver, R. (2004) Results
305 from a McCrone spindle stage short course, a new version of EXCALIBR, and how to build a
306 spindle stage. The Microscope, 52, 23–39.
307 Gurzhiy, V.V., and Plášil, J. (2019) Structural complexity of natural uranyl sulfates. Acta
308 Crystallographica, B75, 39–48.
309 Higashi, T. (2001) ABSCOR. Rigaku Corporation, Tokyo.
310 Kampf, A.R., Plášil, J., Kasatkin, A.V., Marty, J., and Cejka, J. (2015) Fermiite,
311 $Na_4(UO_2)(SO_4)_3$-$3H_2O$ and oppenheimerite, $Na_2(UO_2)(SO_4)_2 \cdot 3H_2O$, two new uranyl sulfate
312 minerals from the Blue Lizard mine, San Juan County, Utah, USA. Mineralogical Magazine,
313 79, 1123–1142.
314 Krivovichev, S.V. (2012): Topological complexity of crystal structures: quantitative approach.
315 Acta Crystallographica, A68, 393–398.
316 Krivovichev, S.V. (2013): Structural complexity of minerals: information storage and processing
317 in the mineral world. Mineralogical Magazine, 77, 275–326.
318 Krivovichev, S.V. (2014): Which inorganic structures are the most complex? Angewandte
319 Chemie, International Edition English, 53, 654–661.

Krivovichev, S.V. (2018): Ladders of information: what contributes to the structural complexity of inorganic crystals. Zeitschrift für Kristallographie, 233, 155–161.

Libowitzky, E. (1999) Correlation of O-H stretching frequencies and O-H···O hydrogen bond lengths in minerals. Monatshefte für Chemie, 130, 1047–1059.

Lussier A.J., Lopez R.A.K., and Hawthorne, F.C. (2016) A revised and expanded structure hierarchy of natural and synthetic hexavalent uranium compounds. Canadian Mineralogist, 54, 177–283.

Mandarino, J.A. (1976) The Gladstone-Dale relationship – Part 1: derivation of new constants. Canadian Mineralogist, 14, 498–502.

Mandarino, J.A. (2007) The Gladstone–Dale compatibility of minerals and its use in selecting mineral species for further study. Canadian Mineralogist, 45, 1307–1324.

Plášil, J., Kampf, A.R., Kasatkin, A.V., Marty, J., Škoda, R., Silva, S., and Čejka, J. (2013) Meisserite, $Na_5(UO_2)(SO_4)_3(SO_3OH)(H_2O)$, a new uranyl sulfate mineral from the Blue Lizard mine, San Juan County, Utah, USA. Mineralogical Magazine, 77, 2975–2988.

Plášil, J., Kampf, A.R., Kasatkin, A.V., and Marty, J. (2014) Bluelizardite, $Na_7(UO_2)(SO_4)_4Cl(H_2O)_2$, a new uranyl sulfate mineral from the Blue Lizard mine, San Juan County, Utah, USA. Journal of Geosciences, 59, 145–158.

Pouchou, J.-L., and Pichoir, F. (1991) Quantitative Analysis of Homogeneous or Stratified Microvolumes Applying the Model "PAP." Pp. 31–75 in: Electron Probe Quantitation. Springer US, Boston, MA.

Qiu, J., Spano, T.L., Dembowski, M., Kokot, A.M., Szymanowski, J.E.S., and Burns, P.C. (2017) Sulfate-centered sodium-icosahedron-templated uranyl peroxide phosphate cages with uranyl bridged by μ-η^1:η^2 peroxide. Inorganic Chemistry, 56, 1874-1880.

Sheldrick, G.M. (2015a) SHELXT – Integrated space-group and crystal-structure determination. Acta Crystallographica, A71, 3–8.

Sheldrick, G.M. (2015b) Crystal structure refinement with SHELXL. Acta Crystallographica, C71, 3–8.

Endnote:

[1]Deposit item AM-20-XXXXX, Supplemental tables and CIF. Deposit items are free to all readers and found on the MSA website, via the specific issue's Table of Contents (go to http://www.minsocam.org/MSA/AmMin/TOC/2020/Xxx2020_data/ Xxx2020_data.html).

353 FIGURE CAPTIONS

354

355 Figure 1. Diverging group of seaborgite blades with ferrinatrite. The field of view is 0.68 mm
356 across.

357

358 Figure 2. Crystal drawing of seaborgite; clinographic projection in non-standard orientation.

359

360 Figure 3. The Raman spectrum of seaborgite recorded with a 532 nm laser.

361

362 Figure 4. The observed powder diffraction pattern compared with the pattern simulated from the
363 lines calculated from the crystal structure.

364

365 Figure 5. The $[(UO_2)_2(SO_4)_8]^{4-}$ uranyl sulfate clusters in seaborgite (approx. down [100]) and
366 bluelizardite (down [010]).

367

368 Figure 6. The band along [010] in seaborgite composed of UO_7 pentagonal bipyramids, LiO_4
369 tetrahedra, and SO_4 tetrahedra (S1 thru S4); the S5 SO_4 tetrahedron, which links the bands in the
370 [100] direction is also shown. The view is down [100] and the unit cell outline is shown as
371 dashed lines.

372

373 Figure 7. The thick heteropolyhedral layers parallel to [001] in seaborgite viewed along the chain
374 direction [010]. Note that the S5 SO_4 tetrahedron links the bands in the [100] direction. The unit
375 cell outline is shown as dashed lines.

376

377 Figure 8. The crystal structure of seaborgite viewed down [100]. The K1, K2, and Na/K

378 coordinations are shown ball-and-stick style. The unit cell outline is shown as dashed lines.

379

380

This is the peer-reviewed, final accepted version for American Mineralogist, published by the Mineralogical Society of America.
The published version is subject to change. Cite as Authors (Year) Title. American Mineralogist, in press.
DOI: https://doi.org/10.2138/am-2020-7540. http://www.minsocam.org/

381 Table 1. Chemical analytical results for seaborgite.

Constituent	Mean	Range	Stand. Dev.	Standard	Structure
Li_2O	1.09[§]	1.04-1.11	0.03		1.38*
Na_2O	14.83[§]	14.67-15.00	0.23		
Na_2O	14.34	12.28-15.80	1.14	albite	16.60*
K_2O	8.75	7.95-10.98	0.97	orthoclase	9.50*
UO_3	26.50	24.08-27.96	1.37	syn. UO_2	26.50
SO_3	44.27	42.13-47.57	2.01	anhydrite	44.27
H_2O	2.49*				2.49*
Total	97.93[†] 97.44[‡]				100.74

382 * based upon the structure refinement.
383 [§] measured by LA-ICP-MS
384 [†] using Na measured via EPMA
385 [‡] using Na measured via LA-ICP-MS
386

Table 2. Selected bond distances (Å) and angles (°) for seaborgite.

Li–O20	1.94(2)	Na5–O2	2.337(10)	U–O25	1.754(8)	
Li–O7	1.96(2)	Na5–O21	2.375(11)	U–O26	1.759(8)	
Li–O5	1.97(2)	Na5–O20	2.461(10)	U–O12	2.292(9)	
Li–O17	2.05(2)	Na5–O18	2.476(10)	U–O16	2.360(9)	
<Li–O>	1.98	Na5–O15	2.508(10)	U–O3	2.365(9)	
		Na5–O13	2.573(10)	U–O4	2.377(8)	
Na/K–O6(×2)	2.491(9)	<Na5–O>	2.455	U–O8	2.488(8)	
Na/K–O17(×2)	2.740(10)			<U1–O_{Ur}>	1.757	
Na/K–O5(×2)	2.881(9)	Na6a–O23	2.284(18)	<U1–O_{eq}>	2.376	
Na/K–O7(×2)	3.095(10)	Na6a–O15	2.328(16)			
<Na/K–O>	2.802	Na6a–O13	2.341(15)	S1–O1	1.447(9)	
		Na6a–O22	2.345(19)	S1–O2	1.465(9)	
Na1–OW27(×2)	2.345(11)	Na6a–O11	2.55(4)	S1–O3	1.483(9)	
Na1–O11(×2)	2.394(8)	<Na6a–O>	2.370	S1–O4	1.495(9)	
Na1–O14(×2)	2.534(8)			<S1–O>	1.473	
<Na1–O>	2.425	Na6b–O23	2.271(17)			
		Na6b–O22	2.307(17)	S2–O5	1.458(10)	
Na2–O1	2.311(11)	Na6b–O15	2.342(15)	S2–O6	1.459(9)	
Na2–O2	2.333(9)	Na6b–O13	2.414(17)	S2–O7	1.461(9)	
Na2–O13	2.377(10)	Na6b–O18	2.55(4)	S2–O8	1.502(9)	
Na2–O15	2.415(10)	<Na6b–O>	2.377	<S2–O>	1.470	
Na2–O25	2.415(10)					
Na2–O16	2.768(10)	K1–O1	2.650(9)	S3–O9	1.447(9)	
<Na2–O>	2.437	K1–O3	2.799(8)	S3–O10	1.475(8)	
		K1–O5	2.799(9)	S3–O11	1.476(9)	
Na3–O10	2.379(10)	K1–O17	2.809(10)	S3–O12	1.499(9)	
Na3–O14	2.412(10)	K1–O2	2.818(9)	<S3–O>	1.474	
Na3–OW27	2.434(11)	K1–O26	2.840(9)			
Na3–O9	2.502(10)	K1–O8	2.971(9)	S4–O13	1.450(9)	
Na3–O22	2.567(10)	K1–O6	2.979(9)	S4–O14	1.452(9)	
Na3–O11	2.590(10)	<K1–O>	2.833	S4–O15	1.463(8)	
Na3–O23	2.658(11)			S4–O16	1.502(9)	
<Na3–O>	2.506	K2–O21	2.755(9)	<S4–O>	1.467	
		K2–O10	2.764(9)			
Na4–O9	2.302(10)	K2–O22	2.765(9)	S5–O17	1.454(10)	
Na4–O10	2.313(10)	K2–O9	2.889(9)	S5–O18	1.468(9)	
Na4–O6	2.450(10)	K2–O20	2.897(10)	S5–O19	1.470(9)	
Na4–O7	2.521(10)	K2–O23	2.897(10)	S5–O20	1.487(9)	
Na4–O19	2.760(11)	K2–O19	2.955(9)	<S5–O>	1.470	
Na4–O8	2.775(10)	K2–O19	2.960(9)			
<Na4–O>	2.520	<K2–O>	2.860	S6–O21	1.411(9)	
				S6–O22	1.444(9)	
Hydrogen bonds				S6–O23	1.458(9)	
D–H···*A*	*D*–H	H···*A*	*D*···*A*	<*D*H*A*	S6–OH24	1.557(10)
OH24–H24···O19	0.82(3)	1.91(5)	2.711(14)	166(15)	<S6–O>	1.468
OW27–H27a···O14	0.82(3)	2.18(5)	2.963(13)	159(12)		
OW27–H27b···O12	0.82(3)	2.35(8)	2.992(14)	135(11)		

Table 3. Bond valence analysis for seaborgite. Values are expressed in valence units.*

	Li	K1	K2	Na/K	Na1	Na2	Na3	Na4	Na5	Na6a	Na6b	U	S1	S2	S3	S4	S5	S6	H bonds	sum
O1		0.22				0.23							1.60							2.05
O2		0.14				0.22			0.22				1.53							2.11
O3		0.15										0.51	1.46							2.12
O4												0.50	1.42							1.92
O5	0.24	0.15		0.08 ×2↓										1.55						2.02
O6		0.10		0.22 ×2↓				0.21						1.55						2.08
O7	0.25			0.05 ×2↓				0.14						1.54						1.98
O8		0.10						0.08				0.39		1.39						1.96
O9			0.12				0.15	0.24							1.60					2.11
O10			0.17				0.20	0.23							1.49					2.09
O11					0.19 ×2↓		0.12			0.14 ×½→					1.49					1.87
O12												0.59			1.40				0.13	2.12
O13						0.20			0.12	0.22 ×½→	0.18 ×½→					1.59				2.11
O14					0.14 ×2↓		0.18									1.58			0.14	2.04
O15						0.18			0.14	0.22 ×½→	0.22 ×½→					1.54				2.08
O16						0.08						0.51				1.39				1.98
O17	0.21	0.15		0.12 ×2↓													1.57			2.05
O18									0.16		0.14 ×½→						1.52			1.75
O19			0.10 0.10					0.08									1.51		0.22	2.01
O20	0.25		0.12						0.16								1.45			1.98
O21			0.17						0.20									1.75		2.12
O22			0.16				0.13			0.22 ×½→	0.24 ×½→							1.61		2.13
O23			0.12				0.10			0.24 ×½→	0.26 ×½→							1.55		2.02
OH24																		1.21	-0.22	0.99
O25						0.18						1.85								2.03
O26		0.14										1.83								1.97
OW27					0.21 ×2↓		0.17												-0.13 -0.14	0.11
sum	0.95	1.15	1.06	0.94	1.08	1.09	1.05	0.98	1.00	1.04	1.04	6.18	6.01	6.03	5.98	6.10	6.05	6.12		

* Bond valence parameters are from Gagne and Hawthorne (2015). Hydrogen-bond strengths are based on O–O bond lengths from Ferraris and Ivaldi (1988).

This is the peer-reviewed, final accepted version for American Mineralogist, published by the Mineralogical Society of America.
The published version is subject to change. Cite as Authors (Year) Title. American Mineralogist, in press.
DOI: https://doi.org/10.2138/am-2020-7540. http://www.minsocam.org/

Figure 1

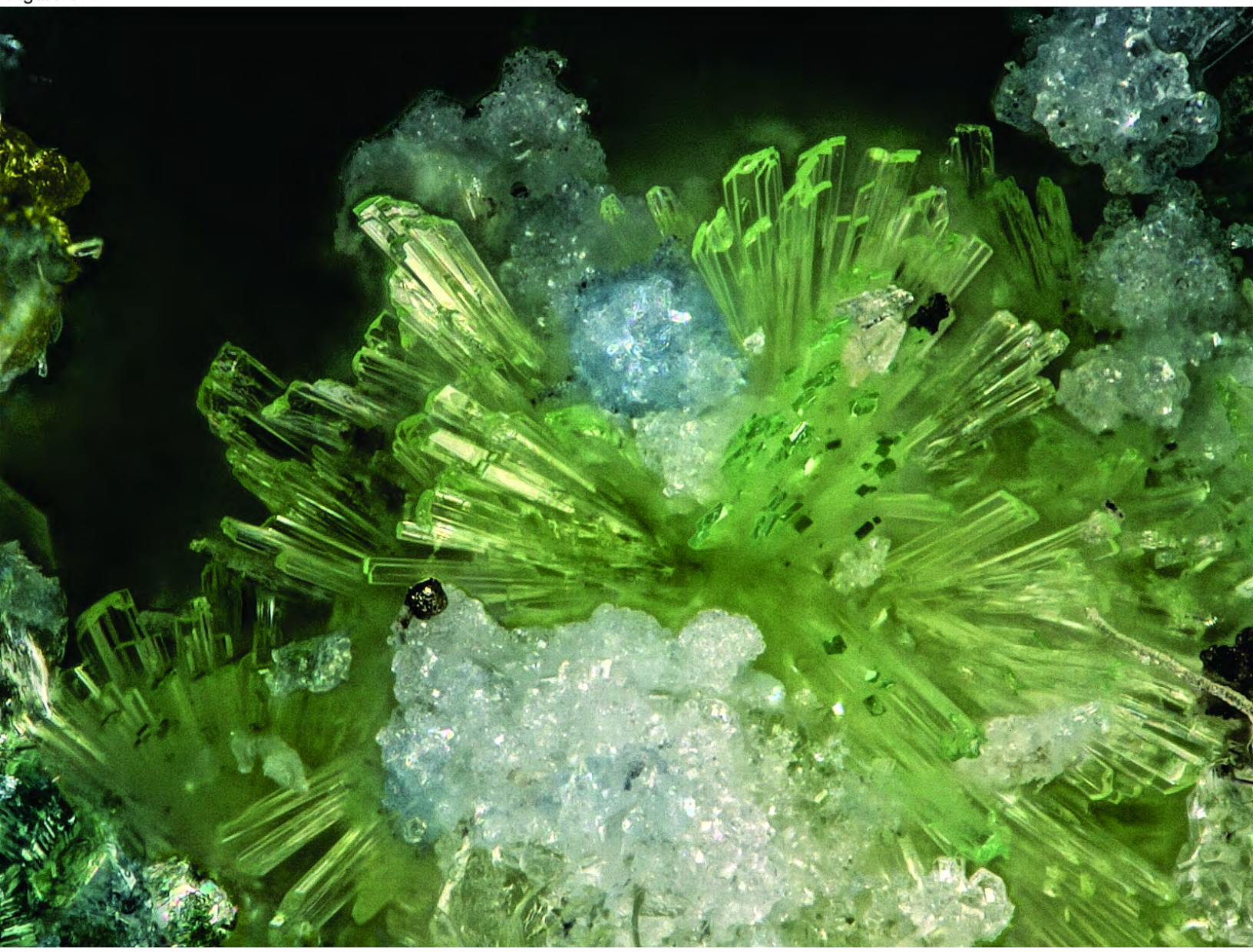

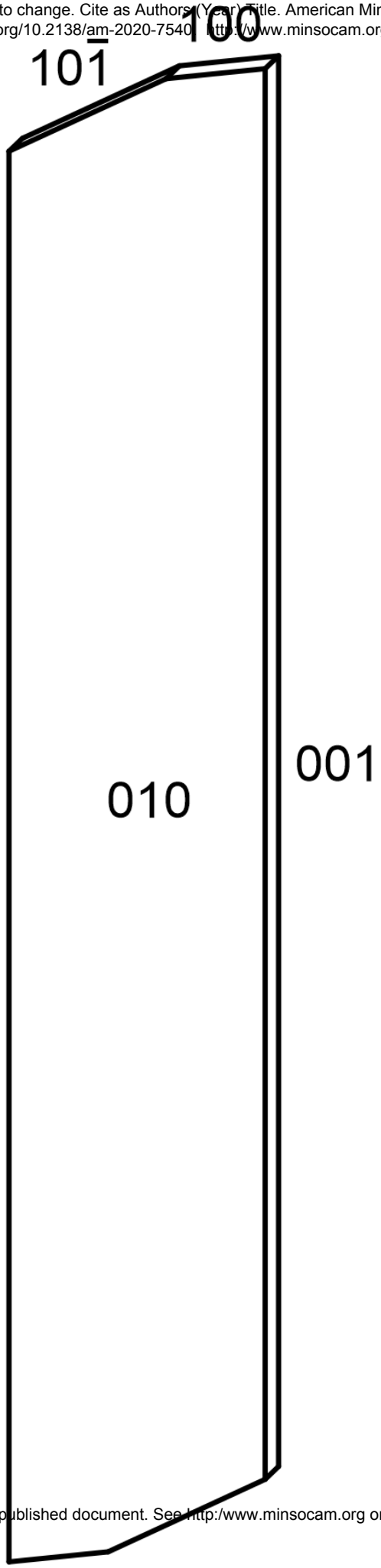

Figure 3

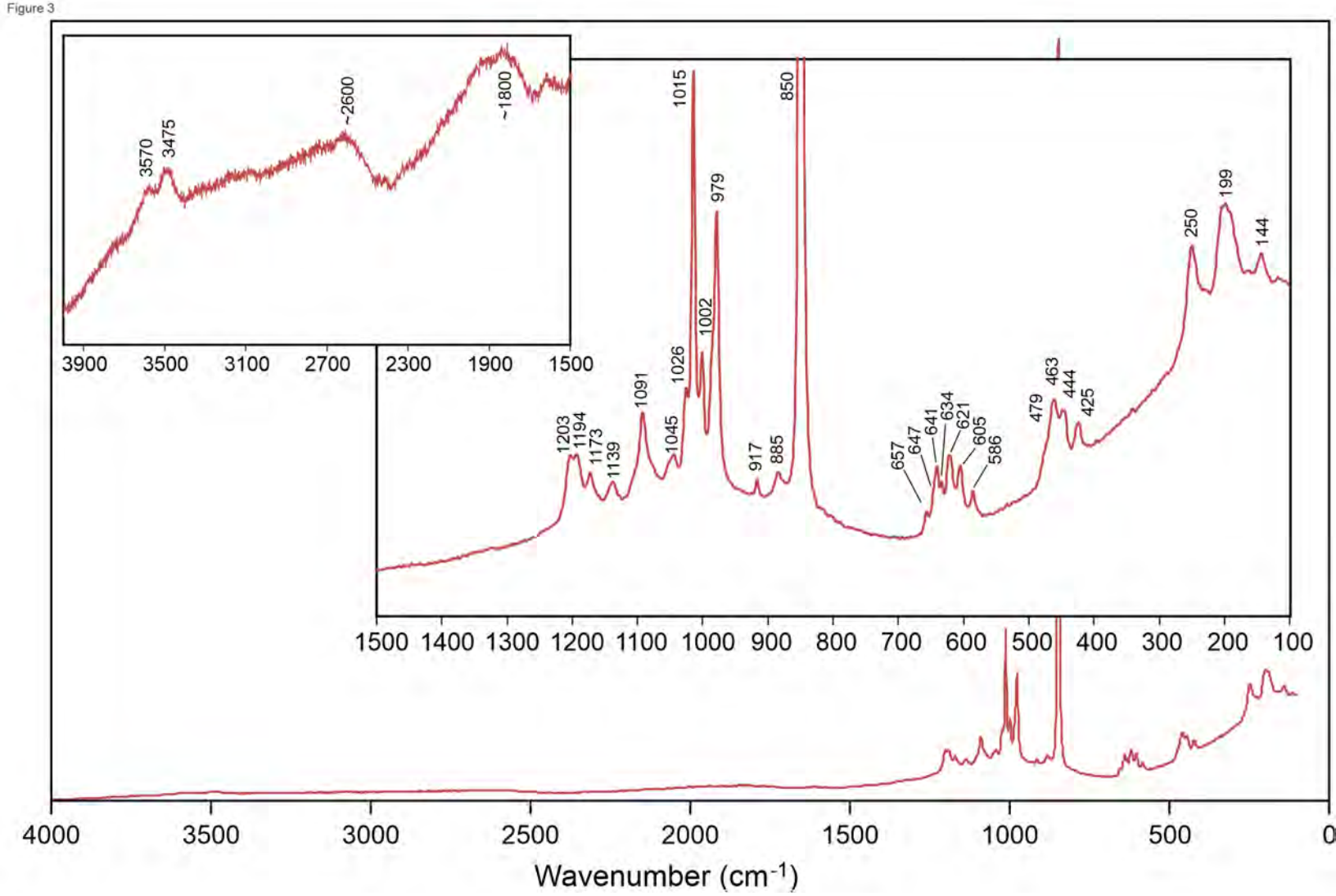

This is the peer-reviewed, final accepted version for American Mineralogist, published by the Mineralogical Society of America.
The published version is subject to change. Cite as Authors (Year) Title. American Mineralogist, in press.
DOI: https://doi.org/10.2138/am-2020-7540. http://www.minsocam.org/

Figure 4

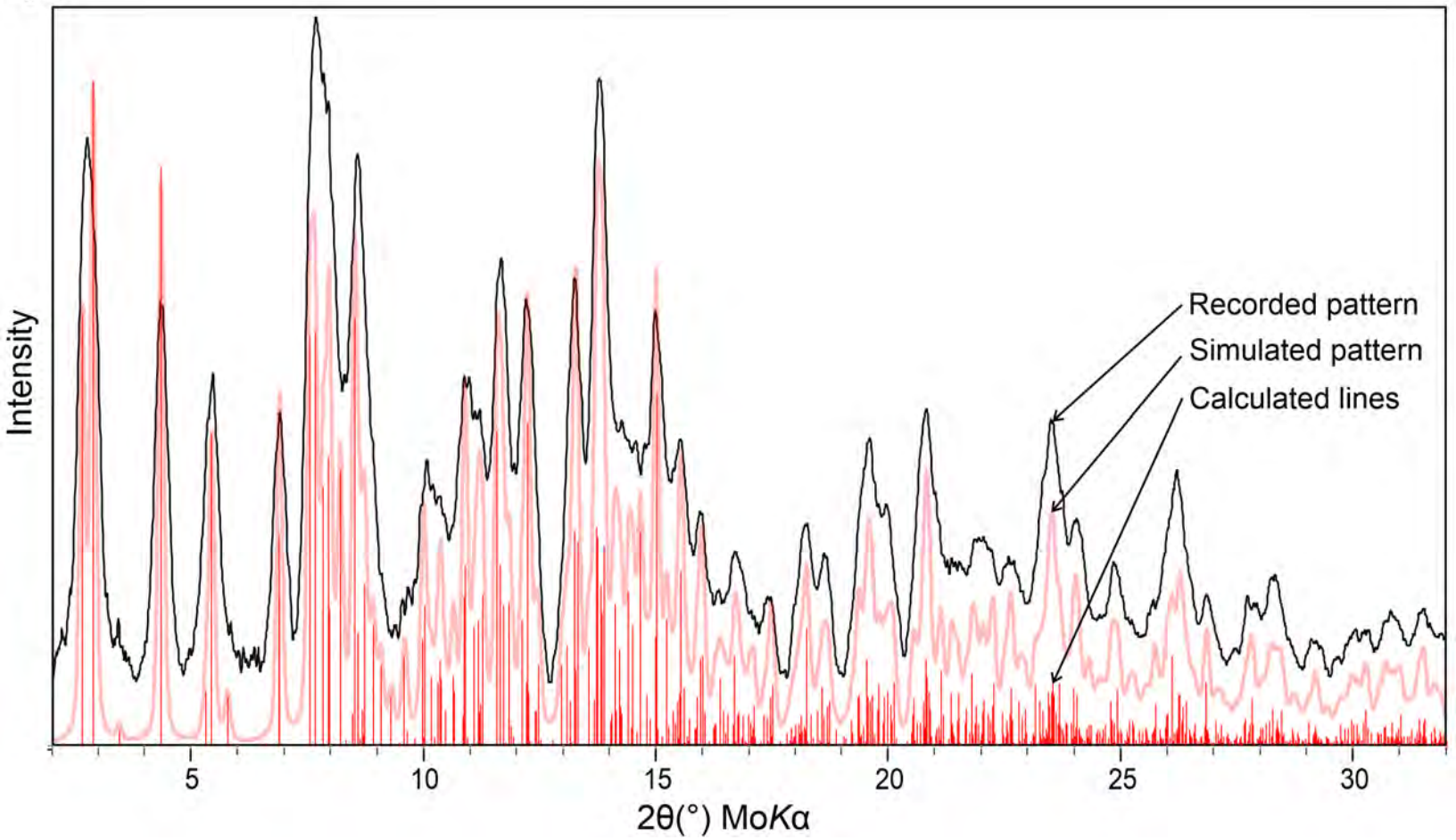

This is the peer-reviewed, final accepted version for American Mineralogist, published by the Mineralogical Society of America.
The published version is subject to change. Cite as Authors (Year) Title. American Mineralogist, in press.
DOI: https://doi.org/10.2138/am-2020-7540. http://www.minsocam.org/

Figure 5

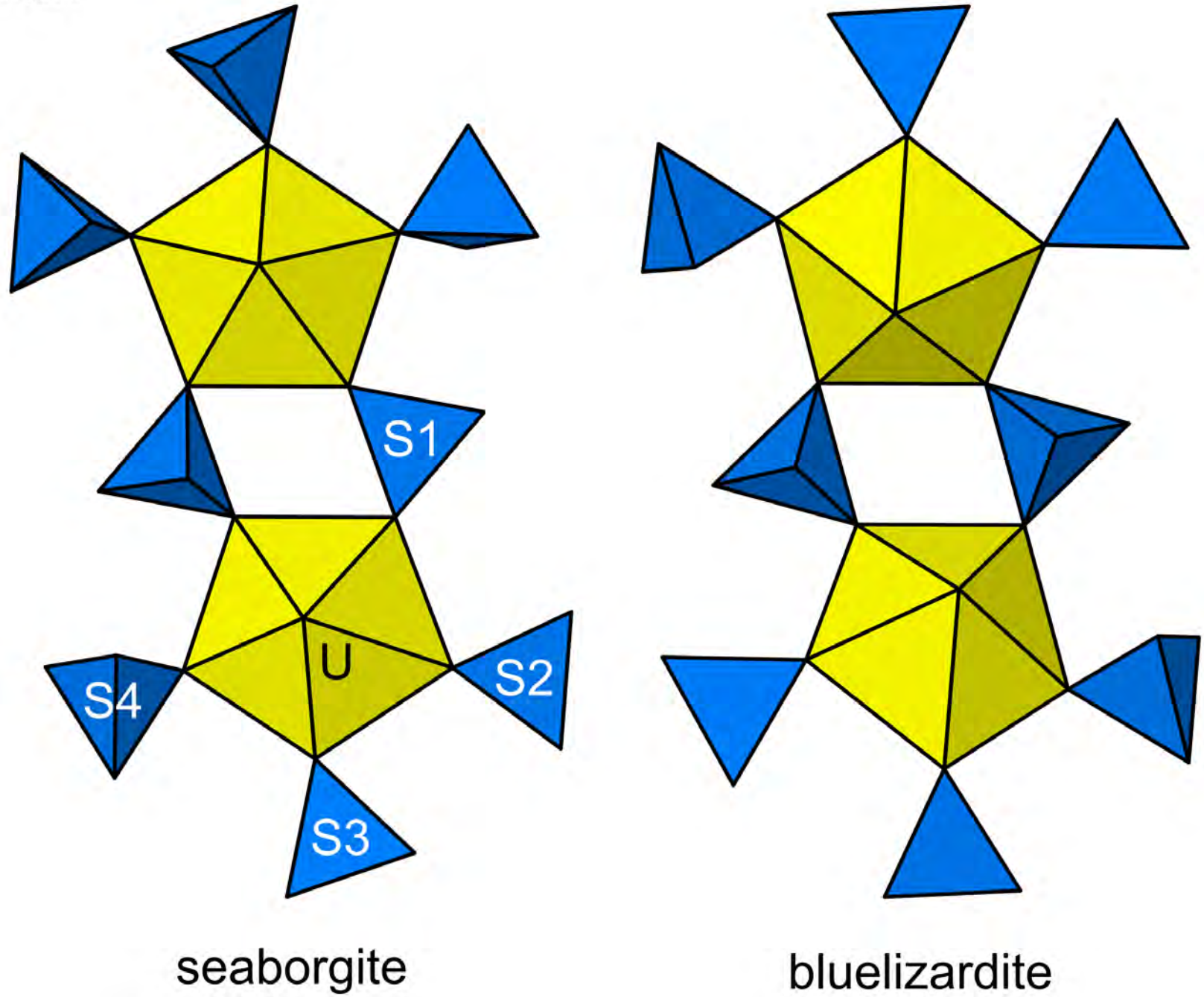

This is the peer-reviewed, final accepted version for American Mineralogist, published by the Mineralogical Society of America.
The published version is subject to change. Cite as Authors (Year) Title. American Mineralogist, in press.
DOI: https://doi.org/10.2138/am-2020-7540. http://www.minsocam.org/

Figure 6

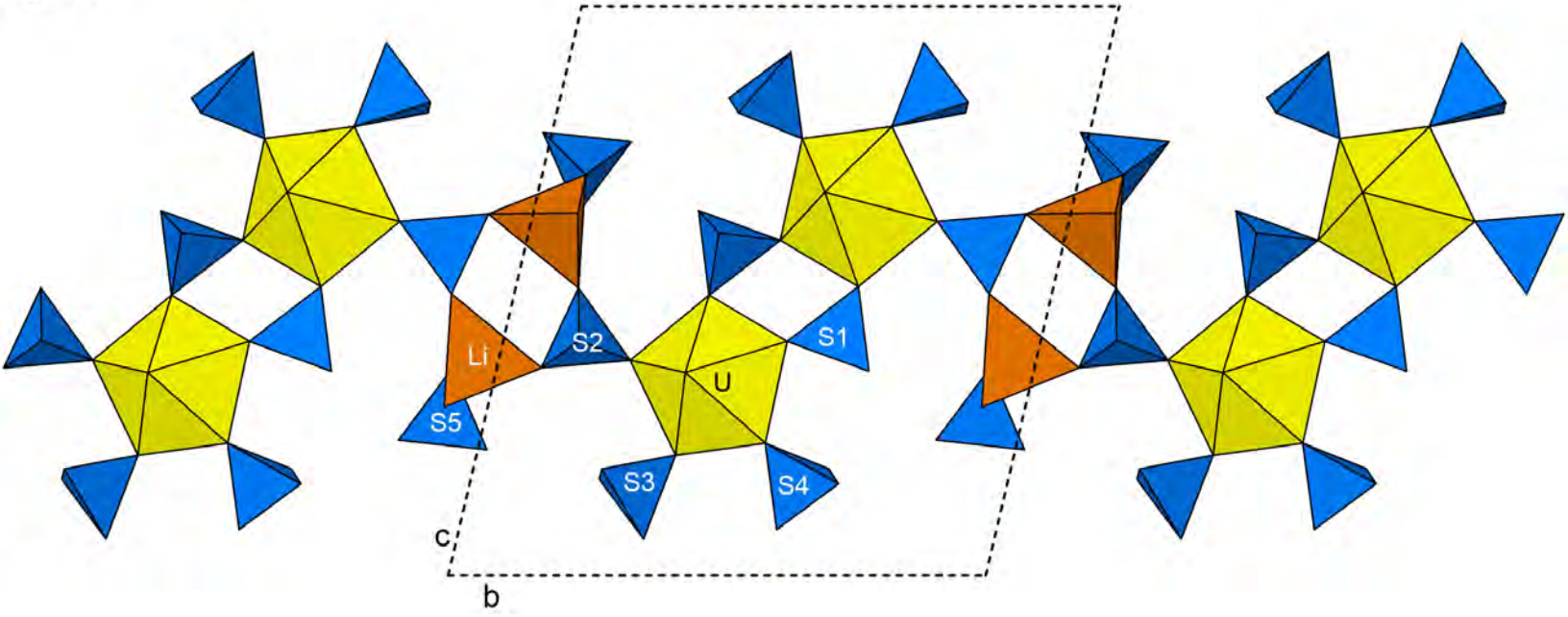

Figure 7

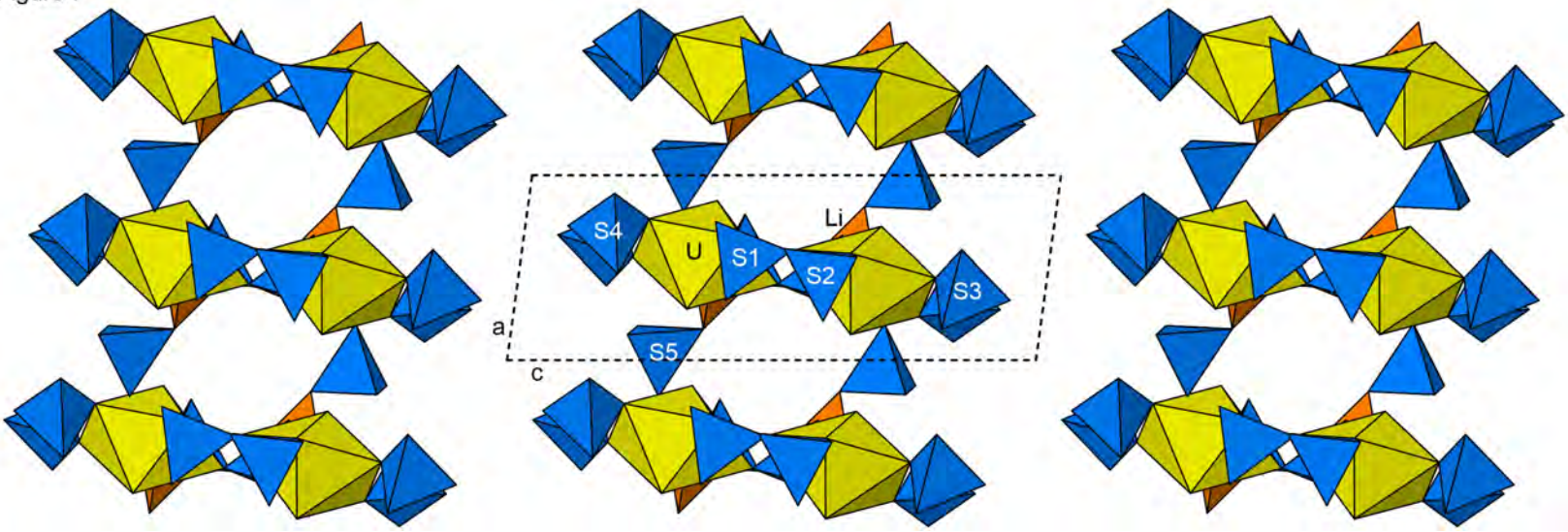

This is the peer-reviewed, final accepted version for American Mineralogist, published by the Mineralogical Society of America.
The published version is subject to change. Cite as Authors (Year) Title. American Mineralogist, in press.
DOI: https://doi.org/10.2138/am-2020-7540. http://www.minsocam.org/

Figure 8